Microwave-Assisted Synthesis of Boron and Nitrogen co-doped Reduced Graphene Oxide for the Protection of Electromagnetic Radiation in Ku-Band

Sima Umrao,[†,§] Tejendra K. Gupta,[†,§] Shiv Kumar,[†] Vijay K. Singh,[†] Manish K. Sultania,[†] Jung Hwan Jung,[‡] Il-Kwon Oh,[‡] and Anchal Srivastava*,[†]

[†]Department of Physics, Banaras Hindu Universisty, Varanasi 221005, India

[‡]Department of Mechanical Engineering, KAIST Institute for the NanoCentury, Korea Advanced Institute of Science and Technology (KAIST), 291 Daehak-ro, Yuseong-gu, Daejeon 305-701, Republic of Korea

S *Supporting Information*

ABSTRACT: The electromagnetic interference (EMI) shielding of reduced graphene oxide (MRG), B-doped MRG (B-MRG), N-doped MRG (N-MRG), and B−N co-doped MRG (B−N-MRG) have been studied in the Ku-band frequency range (12.8−18 GHz). We have developed a green, fast, and cost-effective microwave assisted route for synthesis of doped MRG. B−N-MRG shows high electrical conductivity in comparison to MRG, B-MRG and N-MRG, which results better electromagnetic interference (EMI) shielding ability. The co-doping of B and N significantly enhances the electrical conductivity of MRG from 21.4 to 124.4 Sm^{-1} because N introduces electrons and B provides holes in the system and may form a nanojunction inside the material. Their temperature-dependent electrical conductivity follows 2D-variable range hopping (2D-VRH) and Efros−Shklovskii-VRH (ES-VRH) conduction model in a low temperature range ($T < 50$ K). The spatial configuration of MRG after doping of B and N enhances the space charge polarization, natural resonance, dielectric polarization, and trapping of EM waves by internal reflection leading to a high EMI shielding of −42 dB (∼99.99% attenuation) compared to undoped MRG (−28 dB) at a critical thickness of 1.2 mm. Results suggest that the B−N-MRG has great potential as a candidate for a new type of EMI shielding material useful in aircraft, defense industries, communication systems, and stealth technology.

KEYWORDS: *microwave, reduced graphene oxide, electrical conductivity, variable range hopping, EMI shielding*
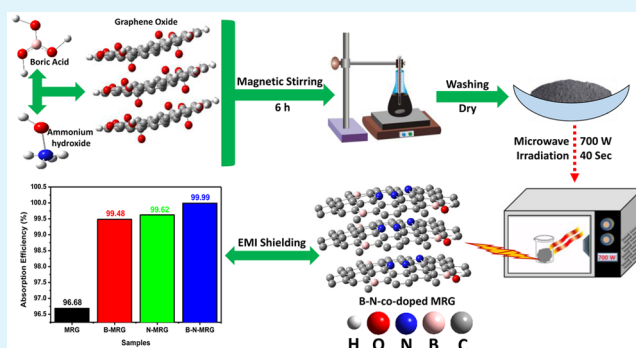
1. INTRODUCTION

Electronic devices such as mobile phones, computers, TV, radio, microwave oven etc. have become an integral part of day-to-day life due to their rapid advancement and ability to make our life easier. However, these devices generate electromagnetic interference (EMI) of radio frequency radiation. This radiation adversely degrades the device performance and is harmful to humans.[1,2] Therefore, there is a need to develop EM shielding materials to prevent EMI pollution. Additionally, EM shielding materials are highly efficient in absorbing EM waves in GHz range in protecting electronic devices associated with the strategic systems, such as aircrafts, nuclear reactors, transformers, control systems, and communication systems from these harmful electromagnetic radiations.[3]

The EMI shielding is strongly related to two important factors: reflection loss and absorption loss. However, reflection loss is the dominating factor for EMI shielding and depends on the interaction between conducting part of the material and the electromagnetic field.[4] While the absorption loss depends on the extent of the absorption of EM waves by the part of

material that has high magnetic permeability.[5] To date, a considerable amount of research has been done to prepare suitable EMI shielding materials by controlling reflection or absorption parameters.

Typically, materials such as metals, dielectrics, magnetic materials, conducting polymers,[6] and different forms of carbon materials such as colloidal graphite,[7] flexible graphite, expanded graphite, carbon fibers, carbon black, single or multiwalled carbon nanotubes (SWCNT or MWCNT), graphene,[2,8] and their composites[9−13] have been widely used as EMI shields due to their high conductivity and good dielectric and magnetic properties.[5] Unfortunately, significant requirements for high EMI shields include not only high conductivity but also light weight, better dispersion, and flexibility. However, the metals have some drawbacks such as being heavy in weight, being susceptible to corrosion, and having complex processing

Scheme 1. Microwave Assisted Approach for the Preparation of B−N Codoped MRG
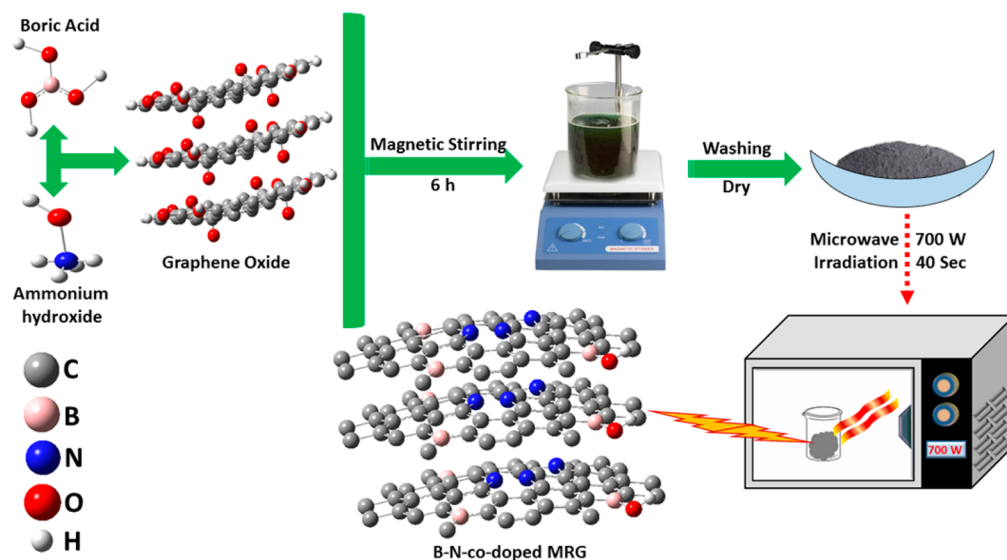
methods and in case of carbon based materials: the poor dispersion, the presence of impurities, lack of interfacial adhesion with other materials and high production costs have marred their use in EMI shielding[2,14] which makes these materials inappropriate for both the researchers and users.

Recently, reduced graphene oxide (RGO) has received much attention as a new class of graphene derivatives due to its many interesting physical and chemical properties such as large surface area, high conductivity, chemical stability, and easy binding ability with other materials.[15,16] It has been proposed that the issues discussed above could be solved by incorporating graphene sheets into polymers for the preparation of composite materials.[17]

Generally, RGO is synthesized by reduction of graphene oxide[17] at high temperature, or by using a reducing agent. But reduction of GO to RGO at high temperature induces high density defects on the edge and basal planes which deteriorates the electrical properties and EMI shielding of RGO.[18,19] Therefore, chemical control of graphene is very important in order to further extend the electrical properties of graphene.[20,21]

With this aim, RGO has been synthesized using microwave assisted reduction of GO because of ease of processability, short time requirement, high yield, no need of hazardous chemicals and special equipment.[18,22] Additionally, to enhance the electrical conductivity of RGO, doping of some p-type and n-type elements (boron, nitrogen etc.) is an effective way of modifying the electrical, chemical, and physical properties.[20,23−25] In particular, doping of boron (B) and nitrogen (N) in graphene results in the disruption of the ideal sp^2 hybridization of the carbon atoms and significant changes in their electronic properties and chemical reactivity.[20,26−28]

There are few works in which the effect of B and N co-doping in graphene[22,29,30] was investigated for several applications. Particularly, Fu et al. reported that B,N-co-doped graphitic carbon shows good oxygen reduction reactions due to the synergistic effect between B and N.[29] Therefore, B and N can be excellent dopants for RGO due to their superiorities like transfer of electron and holes into carbon-based materials and ability to change the electronic and transport properties.[23] Several works have been published on

the synthesis of B- and N-doped graphene for several applications,[22,31−34] but to the best of our knowledge, there are no reports in which B and N co-doped graphene have been synthesized by microwave assisted method and investigated EMI shielding properties.

With this background, the present work provides a novel way to dope B and N in reduced graphene oxide (MRG) and EMI shielding properties have been studied in Ku-band. Ku-band is the small portion of the electromagnetic spectrum in the microwave region of 12−18 GHz. This band is primarily used for satellite communications, Radar and some specific applications such as tracking data relay satellites use for both space shuttle and international space station communications.

2. EXPERIMENTAL SECTION

2.1. Materials. Graphite flakes (1−2 mm, NGS Naturgraphit GmbH, Germany), potassium permanganate (KMnO$_4$, ≥ 99.0%, Fluka), ethanol (CH$_3$CH$_2$OH, ≥ 98% Sigma-Aldrich), boric acid (H$_3$BO$_4$, ≥ 98% Sigma-Aldrich), ammonia solution, H$_2$SO$_4$, H$_3$PO$_4$, H$_2$O$_2$ and H$_6$N$_2$O etc. from Merck India were used.

2.2. Synthesis of Graphene Oxide and Reduced Graphene Oxide. Graphene oxide (GO) have been synthesized using chemical route as suggested by Marcano et al.[35] with some modifications, as briefly described here. Initially, 2 g of graphite flakes were added to concentrated H$_2$SO$_4$/H$_3$PO$_4$ (9:1) solution and stirred on a magnetic stirrer followed by slow addition of 6 weight equivalent of KMnO$_4$ (12 g). Addition of KMnO$_4$ should be very slow to avoid any kind of explosion. The mixture was stirred for 12 h at a constant temperature of 50 °C. Afterward, the mixture was cooled to room temperature and the reaction was quenched by adding ca. 270 mL of ice with slow addition of 2 mL H$_2$O$_2$ (30%) as the reaction is highly exothermic. The mixture was then filtered, shifted, and centrifuged. The obtained solid material was washed with distilled water, 30% HCl and ethanol until the pH ≈ 7 was reached. The material was then dried at 80 °C. Finally, the exfoliated graphene oxide dispersion was obtained for further experiments. The conversion of GO to reduced graphene oxide (MRG) was achieved using microwave-assisted thermal expansion method by microwave irradiation of 700 W for 40 s.

2.3. Preparation of Boron, Nitrogen and B−N co-doped MRG. Boron doped MRG (B-MRG) was prepared using simple chemical mixing-as briefly described here. 500 mg of GO was well dispersed in ethanol (50 mL) using both bath and ultra sonicator.

A transparent solution of boric acid (200 mg) in water (1 mg/mL) was also prepared. Boric acid solution was then added to GO

dispersion under stirring condition and kept at 60 °C for 8 h for completion of reaction. The reaction mixture was then cooled to room temperature. The mixture has been washed using hot DI water to remove unreactive boric acid[36] and then dried at 80 °C. Obtained solid material was then exfoliated using a microwave oven at 700 W for 40 s and found lightweight cotton like black powder of B-MRG. In the similar way, nitrogen doped MRG (N-MRG) has been synthesized using ammonia solution (200 mL).

B−N co-doped MRG (B−N-MRG) was also synthesized by adding ammonia solution and boric acid solution simultaneously under vigorous stirring condition and following the similar above written process as B-MRG and N-MRG, which is also shown in Scheme 1.

2.4. Materials Characterizations. The surface morphology of doped and undoped graphitic samples was examined using scanning electron microscope (SEM, Nova 230, FEI, Netherlands) and microstructural properties were investigated using transmission electron microscopes (TEM, Technai G2 F30 S-Twin, FEI, Nether-lands). High-resolution X-ray photoelectron spectroscopy (XPS) results were obtained using a Multi-Purpose Sigma Probe, Thermo VG Scientific system. Raman studies were carried out using Renishaw inVia micro-Raman spectrometer with an excitation source of 532 nm. The XRD patterns were recorded using high power normal and micro X-ray Diffractometer (XPERT-PRO, λ = 1.5405980 Å) in the diffraction (2θ) range of 10−80°. The analysis of attached functional groups in doped and undoped MRG samples was done by Fourier transform infrared (FT-IR) Spectrometer (65 FT-IR, PerkinElmer). The electrical conductivity of all the samples was measured using conventional four probe system. EMI shielding effectiveness (SE) was measured using a vector network analyzer (VNA E8263B Agilent Technologies). The powder samples were pelletized in a rectangular shape having dimensions 15.8 × 7.9 mm^2 of thickness ~1.2 mm and placed inside a copper sample holder connected between the waveguide flanges of the network analyzer in the Ku-band (12.4−18.0 GHz) waveguide.

3. RESULTS AND DISCUSSION

The synthesis route of B−N-MRG has been described in Scheme 1. Microwave reduction initiated few layered graphene with B and N dopant. Surface morphologies of MRG, N-MRG, B-MRG, and B−N-MRG have been shown in Figure 1. The layered structure of graphene is clearly visible from SEM images, and some slight differences in morphology have been observed after doping (Figure 1d).
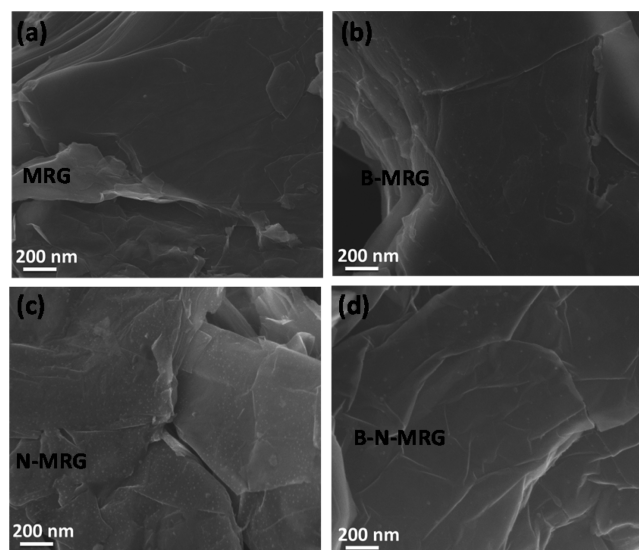

Figure 1. SEM images of (a) MRG, (b) B-MRG, (c) N-MRG, and (d) B−N-MRG.

Further, the morphology and structure of as-prepared MRG and doped MRG were investigated via TEM and HRTEM (Figure 2). TEM images of MRG (Figure 2a,b) show thin, transparent, and layered structure of MRG, and the HRTEM image (inset of Figure 2a) indicates that MRG is composed of five-layer graphitic nanosheets with well-defined interplanar spacing of 0.35 nm corresponding to (002) plane of graphene. Moreover, the resulting doped MRG sheets are also transparent and layered as observed in the TEM images (Figure 2 c−e), which are even comparable to that of the MRG sheets with slight change may be due to some impurity and defects, which are always present in the system due to imperfection of material production process. In the B−N-MRG sample, some deformation in the graphene structure and slight variation in interlayer spacing is observed in TEM and HRTEM micro-graphs (Figure 2e,f), respectively. Further, it is hard to observe B and N elements in TEM and HRTEM micrographs of B−N-MRG sample because of nearly similar size as C, whereas XPS and FTIR spectra revealed its existence and the effects of doping were further confirmed by Raman Spectra.

Typical X-ray diffraction (XRD) patterns of MRG, N- MRG, B- MRG, and B−N-MRG have been shown in Figure 3a. In the diffraction pattern of MRG, the peak around 26.13° (interlayer spacing (d) = 0.35 nm) corresponds to the (002) reflection of graphitic structure in stacked graphene sheets, while the other peak at 43.7° (d = 0.208 nm) having lower intensity corresponds to the (100) reflection implying the formation of turbostatic graphitic carbon.[37] The strong (002) graphitic peak at 26.13° indicates a high crystalline degree for all the doped and undoped MRG samples.

Lattice parameter of the samples have been calculated using the formula[38]

$$\sin^2 \theta = \frac{\lambda^2}{4} \left[\frac{4}{3} \left(\frac{(h^2 + hk + k^2)}{a^2} \right) + \frac{l^2}{c^2} \right]$$

(1)

where θ is the diffraction angle, λ is incident wavelength (λ = 1.5406 Å), and h, k, and l are Miller's indices. Interplanar spacing is calculated by using the formula[38]

$$\frac{1}{d^2} = \frac{4}{3} \left(\frac{h^2 + hk + k^2}{a^2} + \frac{l^2}{c^2} \right)$$

(2)

The average crystallite size (D) of the samples are estimated using the Debye−Scherrer's equation[38]

$$D = \frac{0.9\lambda}{\beta \cos \theta}$$

(3)

where λ the wavelength of radiation used (λ = 1.5406 Å), θ is the Bragg angle, and β is the line broadening at half of the maximum intensity (fwhm) after subtracting the instrumental line broadening in radians. The interplanar spacing of d_{002} plane, crystallite size, and lattice parameters of all samples calculated from above equations show nonremarkable varia-tions which are shown in Table 1.

Furthermore, Fourier transform infrared (FT-IR) spectra of the MRG, B-MRG, N-MRG, and B−N-MRG were measured to study the effect of doping on chemical structure as shown in Figure 3b. We can easily recognize from the Figure 3b that the various new vibrational bonds such as C−N (1051 cm^{-1}), B−C (1326 cm^{-1}) and B−O (620 cm^{-1}) are present after doping of N and B. The peak at ~1630 cm^{-1} corresponds to C≡C stretching, and the peak at ~1390 cm^{-1} is due to C−O bond.
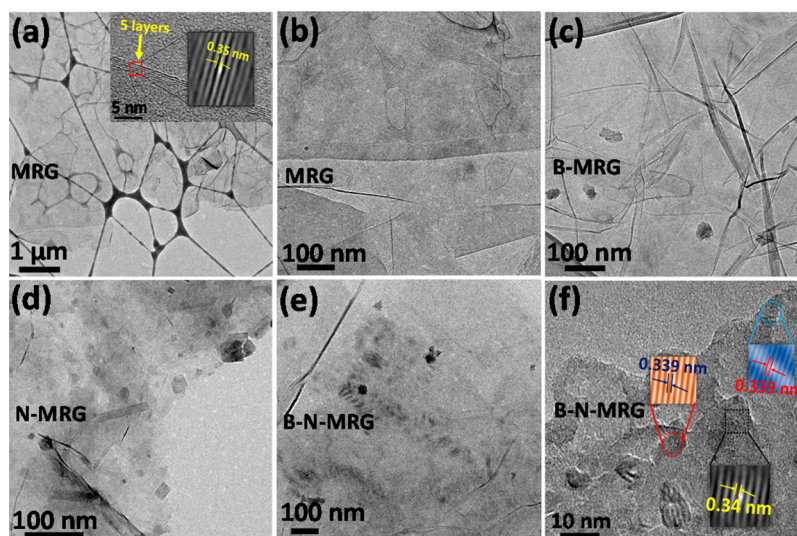
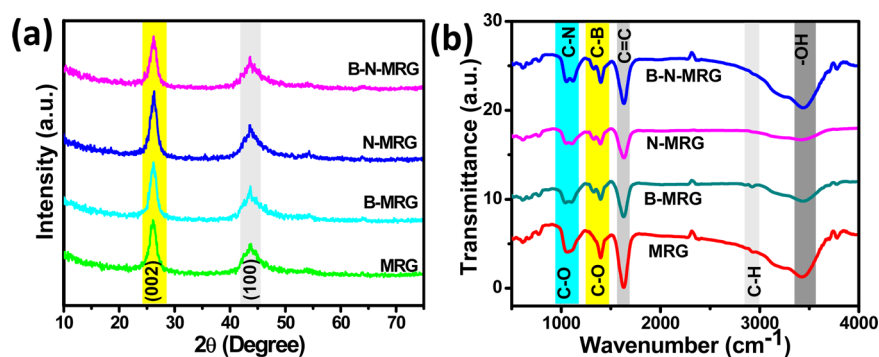**Figure 2.** TEM images of (a and b) MRG, (c) B-MRG, (d) N-MRG, and (e) B−N-MRG. (f) HRTEM of B−N-MRG.

Figure 3. (a) XRD diffraction patterns and (b) FTIR spectrum of MRG, B-MRG, N-MRG and B−N-MRG.

Table 1. Lattice Parameter, Inter-Planar Spacing and Crystallite Size

parameters	samples			
	MRG	B-MRG	N-MRG	B−N-MRG
a (Å)	2.3805	2.3759	2.3748	2.3930
c (Å)	6.8278	6.8098	6.7970	6.8073
d_{100} (Å)	2.0616	2.0575	2.0566	2.0724
d_{002} (Å)	3.4139	3.4049	3.3985	3.4036
crystallite size (nm)	5.48	5.77	5.52	5.47

To study the elemental composition, we investigated the doping effects of B and N in MRG by XPS analysis. XPS survey (Figure S2, Supporting Information) shows the presence of B and N with C and O elements in B−N-MRG and the composition of C, O, B, and N elements (in atomic %) has been found to be 83.13, 15.34, 1.03, and 0.5, respectively. Figure 4a shows the core level spectra of C 1s for the MRG with its deconvoluted three peak positions observed at binding energies of 284.6, 286.01, and 287.5 eV, corresponding to sp^2C−sp^2C, C−O, and C−OH bonds, respectively.[39] For the B−N-MRG (Figure 4b), the C 1s core level spectra can be deconvoluted into five components peaks at 283.8, 284.5, 285.4, 286.5, and 288.9 eV corresponding to C−B, sp^2C−sp^2C, N−sp^2C, N−sp^3C, and −COOH bonds, respectively.[29,40]

The N 1s core level spectra (Figure 4c) can also be deconvoluted into three components centered at 398.1, 399.1,

and 401.3 eV corresponding to pyridinic, pyrrolic, and graphitic type of N atoms doped in the graphene structure, respectively. Similarly, the B 1s core level spectra (Figure 4d) can be deconvoluted into two components centered at 191.9 and 193.1 eV corresponds to B−C and B−O bonds.[29]

Representative Raman spectra of MRG, N-MRG, B-MRG and B−N-MRG have been measured using 532 nm laser excitation. Two-dimensional (2D) contour matrix plot (Figure 5a) for Raman measurements of all samples clearly show D band at ∼1359 cm^{-1}, G band at ∼1586 cm^{-1}, 2D band at ∼2700 cm^{-1}, and D+Ḋ band at ∼2945 cm^{-1}. The D band is originated due to a breathing mode of A_{1g} symmetry, which is endorsed to the presence of disorder in graphene sheets.

The G band is a doubly degenerate phonon mode (E_{2g} symmetry) of sp^2 carbon network, which shows the graphitic nature of compound.[41] The 2D band is overtone of D band and very sensitive to the stacking order of graphene layers resulting in turbostatic graphite, which lacks a stacking order and is considered 2D graphite. In multilayers graphene, 2D band consists of two sub-bands at 2688 ± 0.70 cm^{-1} and 2720 ± 0.20 cm^{-1} (Figure 5b), which are attributed to contributions from 2D graphite and the highly oriented 3D structure of graphite, respectively.[42] Since the 2D band originates from a process where two phonons with opposite wave-vectors satisfy momentum conservation, no defects are required for the activation of 2D bands and that is why this peak is always present in all samples. On the other hand, the D+D′ band is
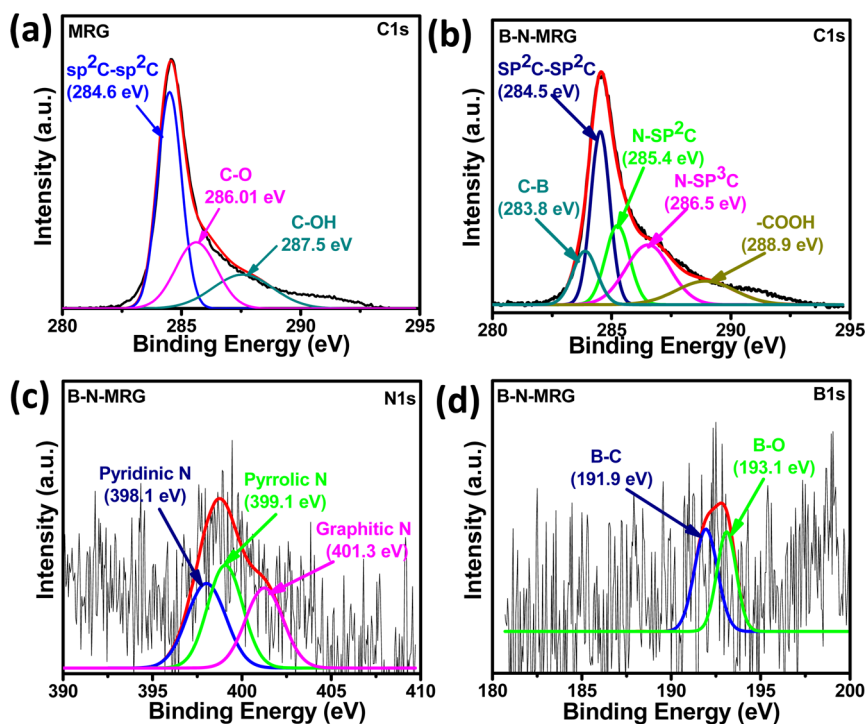
Figure 4. XPS spectra: (a) C 1s core−shell spectra of MRG, (b) C 1s core−shell spectra of B−N-MRG, (c) N 1s core−shell spectra of B−N-MRG, and (d) B 1s core−shell spectra of B−N-MRG.
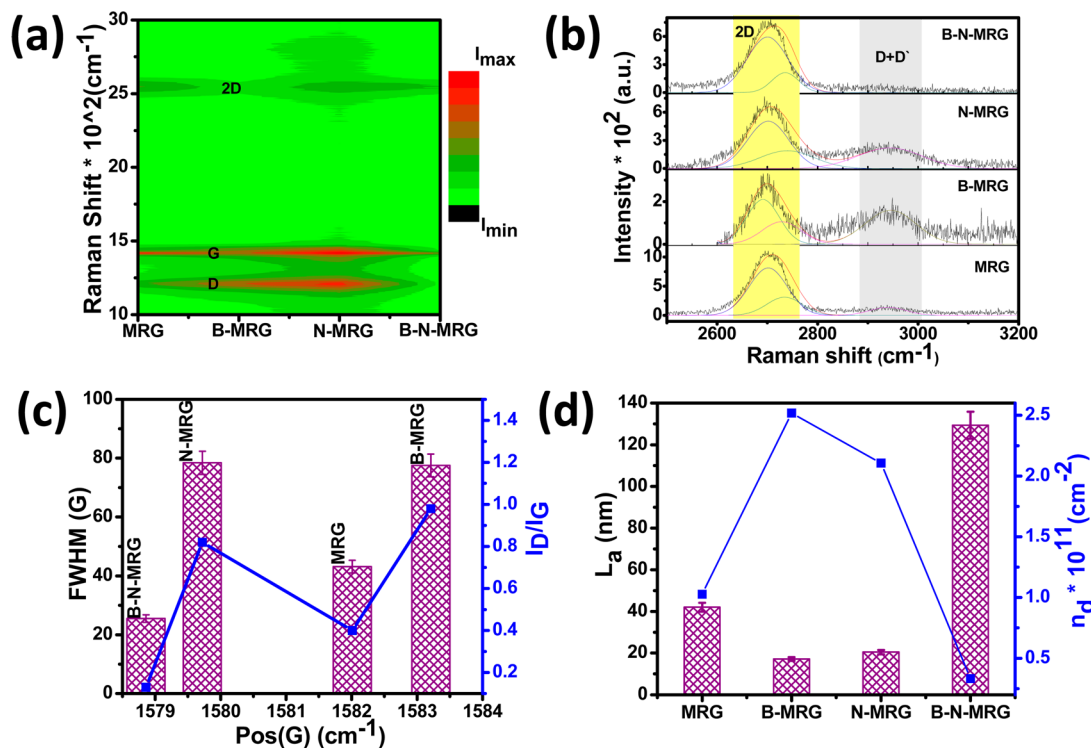

Figure 5. (a) 2D contour mapping of RAMAN spectrum for all synthesized samples, (b) Gaussian peak fitted plot for 2D and D+D′ peak, (c) plot of Pos (G) versus fwhm of G band, and (d) a plot for density of defects (n_d) and distance between defects (L_a).

originated due to the combination of phonons with different momenta around K and Γ, and thus, activation of this band requires defects.[43] From Figure 5d, it is clear that B−N-MRG have less density of defects resulting in disappearance of D+D′ band (Figure 5b) and the distance between defects (L_D) increases in comparison to other samples.

Generally, to identify staging of graphene, the G peak position (Pos (G)) has been widely used.[44,45] Particularly in graphene, the Fermi energy shift has two major effects: (1) variation of the equilibrium lattice parameter, with a consequent softening/stiffening of the phonons[46−48] and (2) the onset of effects beyond the adiabatic Born−Oppenheimer

approximation (BOA), which modify the phonon dispersion close to the Kohn anomalies (KAs).[46,47,49−53] Effect of adiabatic BOA results in an upshift of G band for hole doping (p-type) and a downshift for electron doping (n-type)[46−48] as shown in Figure 5c. Therefore, in the case of B−N-MRG, electron carriers are in excess after co-doping of B and N in comparison to other doped materials.

Density of defects (n_d) and distance between defects (L_D) have also been calculated in order to understand the role of defects which ultimately affect the mobility of charge carriers as shown in Figure 5 (d). L_D for the MRG and doped MRG samples based on Raman data were calculated using the following Equation.[54]

$$L_D(nm) = (2.4 \times 10^{-10}) \times \lambda^4 \left(\frac{I_D}{I_G} \right)^{-1}$$

(4)

where λ (~532 nm) is the wavelength of the excitation laser, and I_D/I_G represents the intensity ratio of the D and G peaks. The density of defects varies inversely to square of distance between defects and is calculated using formula:

$$n_d(nm) = (1.8 \mp 0.5) \times 10^{22} \frac{1}{\lambda^4} \left(\frac{I_D}{I_G} \right)$$

(5)

Electrical properties of MRG, B-MRG, N-MRG, and B−N-MRG samples were investigated as a function of temperature using four probe system. Electrical conductivity of all samples was measured at room temperature and it increases from 21.4 Sm^{-1} for MRG to 124.4 Sm^{-1} for B−N co-doped MRG as shown in Figure 6.
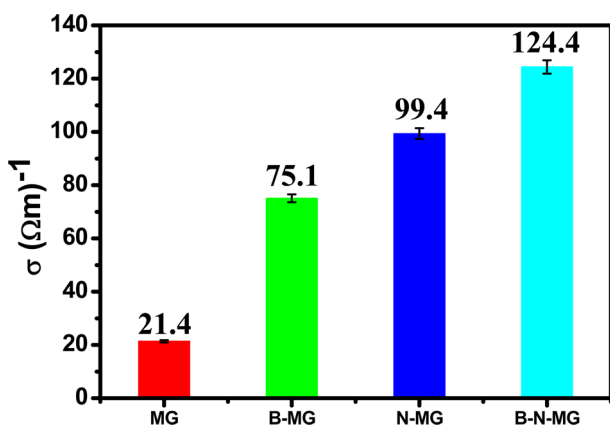

Figure 6. Electrical conductivity of MRG, B-MRG, N-MRG and B−N-MRG at room temperature.

For co-doped MRG, the N or B doping brings great modifications in the graphene sheet which has already been confirmed by TEM, XPS, RAMAN, and XRD results. It is well-known that N introduces free electrons and B imparts holes to graphene sheets, and both processes promote electron transfer between valence and conduction bands and hence greatly improve the electrical conductivity.[55]

The N doping brings about an atomic scale structural deformation[56] resulting in new chemical structures such as pyridinic, pyrrolic and graphitic nitrogen in graphene sheet which is confirmed by XPS while the B doping leads to the formation of C−B bond in the graphene sheets. N atoms can act as an electron donor and increase the n-type conductivity of

graphite structure due to its high electronegativity (3.04 in Pauling scale) compared to C (2.55 in Pauling scale). Moreover, B atom has close electronegativity (2.04 in Pauling scale) to C atom and the C−B bonds are predominately at the edge or defect sites, which may cause the conductivity enhancement. N and B co-doping enhance the conductivity of graphene by introducing free electrons and holes into host graphene π-conjugation systems, which may create a junction within graphene layers and this type of nanojunction may act as nanodevices.[55]

Further, electrical conductivity of all samples has been studied for a complete temperature range of 20−300 K. Nonlinear behavior of resistance with temperature was observed for all samples. Thermally activated transport and variable range hopping models have been used to explain the mechanism for the nonlinear variation of resistance with temperature. These two conduction mechanism have been attested by the plot of ln (ρ) versus 1000/T, which shows two different slopes in the low and high temperature regions (Figure 7a,b).

In the high-temperature region ($T > 50$ K), ln (ρ) versus 1000/T plot was best fitted by a straight line which is characteristic of thermal activation mechanism dominated Arrhenius-like temperature dependence. The thermally activated resistivity follows the Arrhenius law given as

$$\rho(T) = \rho_0 \exp\left[\frac{E_a}{k_B T} \right]$$

(6)

Where k_B is the Boltzmann constant and E_a is the activation energy.

With the straight line fit to Arrhenius plot shown in Figure 7a,b, activation energies have been calculated in the order of 3.283, 2.378, 3.08, and 1.98 meV for MRG, B-MRG, N-MRG, and B−N-MRG, respectively. The resistivity behavior in region ($T < 50$ K) is described by the electric conduction model developed by Mott for the conduction in disordered materials[57] due to the variable range hopping of polaron at low temperature.

In an effort to identify the dominant charge transport mechanism, we attempted to fit the four-probe resistivity data with the Mott VRH model given by

$$\rho(T) = \rho_0 \exp\left[\frac{T_0}{T} \right]^{1/d+1}$$

(7)

where d is the dimensionality of the system ($d = 2$ for two-dimension system), ρ_0 is the pre-exponential factor, and T_0 is a constant.

We have found that the data well fitted for 2D VRH model in the low-temperature region. The plot of logarithm of the product of the relative resistance and inverse of square route of corresponding temperature versus $T^{1/3}$ is linear, indicating that the resistivity ($\rho(T)$) obeys Mott 2D VRH model:[58]

$$\rho(T) * T^{-1/2} = \rho_0 \exp\left[\frac{T_0}{T} \right]^{1/3}$$

(8)

where Mott temperature T_0 is[59]

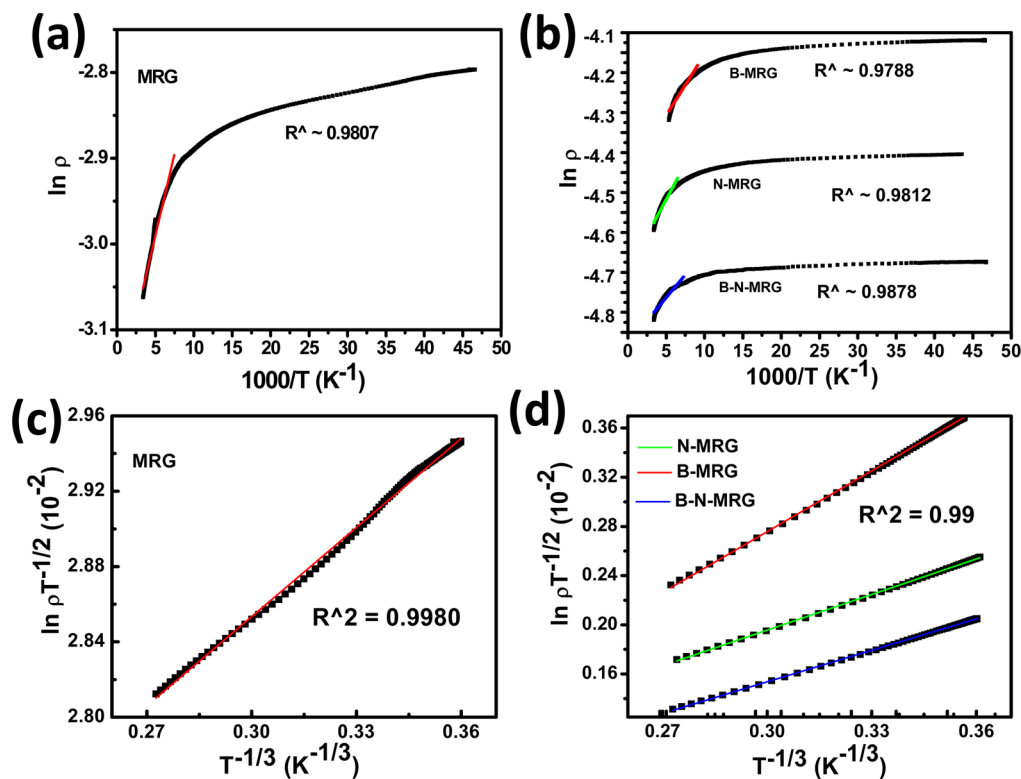$$T_0 = \left[\frac{13.8\alpha^2}{k_B N(E_F)} \right]$$

(9)

Figure 7. Thermally activated resistivity follow Arrhenius plot; ln ρ versus 1000/T for (a) MRG, (b) B-MRG, N-MRG and B−N-MRG. Mott 2D-VRH model: the plot of ln ρ $T^{-1/2}$ versus $T^{-1/3}$ for (c) MRG, (d) B-MRG, N-MRG, and B−N-MRG.

where α is the inverse localization length, k_B is the Boltzmann constant and $N(E_F)$ is constant density of localized electron states at the Fermi level in 2D given as $N(E_F) \sim 10^{20}$.[60]

The temperatures dependent mean hopping distance and the corresponding hopping energy is given by

$$R_h = \frac{1}{3\alpha}\left[\frac{T_0}{T}\right]^{1/3} \tag{10}$$

and

$$W_h = \frac{1}{3}T_0^{2/3}T^{1/3} \tag{11}$$

The results for all MRG sample (doped and undoped) are well fitted with regression coefficient of ∼0.999 for 2D-VRH model as shown in inset of Figure 7c,d, which indicates that Mott VRH conduction mechanism is dominant below the 50 K.

However, at low temperatures, the effects of Coulomb interaction between electrons are also become relevant. Coulomb interactions between the localized states lead to a soft gap known as Coulomb gap (CG).[59] Then conduction is expected to follow the Efros−Shklovskii (ES)-VRH model for 2D materials[61] at low temperature and obeys the following formula:

$$\rho(T) = \rho_0 \exp\left[\frac{T_{ES}}{T}\right]^{1/2} \tag{12}$$

The plot of lnρ $T^{-1/2}$ versus $T^{1/2}$ for all sample are well fitted with regression coefficient of ∼0.99 as shown in Figure 8, indicating that the resistivity ($\rho(T)$) obeys ES-VRH model. The inverse localization length can be directly calculated by using the equation
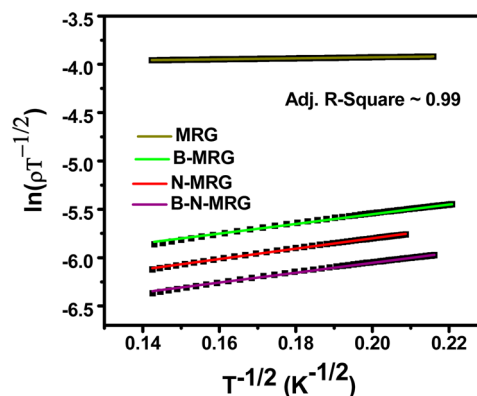

Figure 8. ES-VRH plot at low temperature for MRG, B-MRG, N-MRG and B−N-MRG.

$$T_{ES} = \left[\frac{\beta e^2 \alpha}{4\pi \varepsilon \varepsilon_0 k_B}\right] \tag{13}$$

where $\beta \sim 2.8$ is a constant,[61] ε is the permittivity of vacuum and $\varepsilon_0 \sim 3.5$ is the dielectric constant of RGO.[62]

Furthermore, the hopping energy (W_h), hopping distance (R_h) and coulomb gap energy (E_{CG}) have been calculated using following equations:

$$R_h = \frac{1}{4\alpha}\left[\frac{T_{ES}}{T}\right]^{1/2} \tag{14}$$

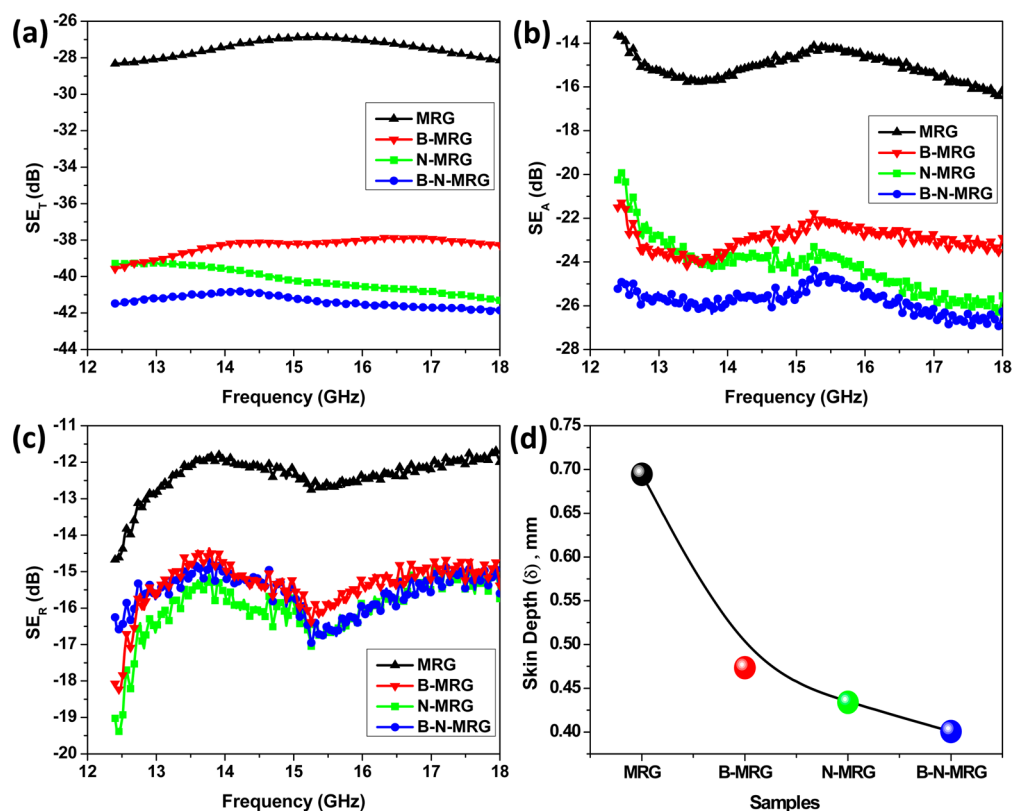$$W_h = \frac{1}{2}T_{ES}^{1/2}T^{1/2} \tag{15}$$

and

Figure 9. (a) Frequency dependent total EMI shielding (SE$_T$), (b) EMI shielding due to absorption (SE$_A$), (c) EMI shielding due to reflection (SE$_R$), and change in skin depth of B, N doping and B−N co-doping in MRG (d).

$$E_{CG} = \frac{T_{ES}}{(\beta)(\sqrt{4\pi})} \tag{16}$$

Various Mott parameters have been calculated using the above-mentioned 2D-VRH model as well as ES-VRH model and shown in Tables S1 and S2.

Further, the remarkable enhancement of electrical conductivity provides a path for better EMI shielding properties in B−N co-doped MRG. EMI shielding is defined as the attenuation of the propagating electromagnetic (EM) waves by the shielding material. In general the efficiency of any shielding material is expressed in decibel (dB). For a higher dB level of EMI shielding, less energy must be transmitted through the shield. It depends upon the reflection, absorption and multiple reflections of the shielding material.[9,14] In case of reflection of radiation, the shield material must have mobile charge carriers like electrons or holes to interact with the electromagnetic radiation. Therefore, the shield material tends to be electrically conducting. However, the absorption ability of shielding material depends on the electric or magnetic dipoles which interact with the electromagnetic radiation. Other than reflection and absorption; multiple reflections is another mechanism of shielding, which refer to the reflection at different interfaces in the shield material. Large surface area or interface area is required in the shied material for multiple reflection mechanism. But the shielding due to multiple reflections can be ignored when the distance between the reflecting surface and interface is large as compared to the skin depth.[10,63] The EM radiations penetrate at high frequencies only near the surface of the conducting material known as skin depth.[10,11] In this study, B and N doped MRG have been prepared and their EMI shielding measurements were carried out in Ku-band frequency range (12.4−18.0 GHz). When electromagnetic radiation is incident on the material, the sum of absorption (A), reflection (R), and transmission (T) must be 1, that is, $T + R + A = 1$.

Figure 9 shows the variation of the shielding effectiveness (SE) with frequency for B-MRG, N-MRG and B−N-MRG samples in 12.4−18 GHz frequency range. The total EMI shielding value (SE$_T$) for B- and N-doped and B−N co-doped MRG is found to be −38, −40, and −42 dB, respectively; these values are quite high compared to undoped MRG (−28 dB at 14.8 GHz frequency) at a thickness of 1.2 mm (Figure 9a). This increase in SE$_T$ is due to dc electrical conductivity. B−N co-doped MRG shows higher electrical conductivity compared to single B and N doped MRG because N doping introduces free electrons and B doping imparts holes to graphene sheets, and both processes promote electron transfer between valence and conduction bands and greatly improved electric conductance. N doping deforms the structure of graphene resulting in a new structure such as pyridinic, pyrrolic, and graphitic nitrogen while B doping leads the formation of C−B bond in the graphene sheets.

In case of B−N co-doping, B and N introduced free electrons and holes simultaneously into host graphene π- conjugation systems and creates a nanojunction within a graphene layers, resulting in enhancement of electrical conductivity, which is much higher than that in single B- and N-doped MRG. This type of deformed structure is further confirmed by Raman spectra which show larger down shift in the G peak of B−N-co-doped MRG compared to single B and N doped MRG.

The enhancement in SE$_A$ is higher than SE$_R$, as shown in Figure 9b,c. However, SE$_R$ is almost constant because the presence of both B and N in MRG enhances the spin

Table 2. Electromagnetic Shielding Properties of Different Graphene Based Materials

| filler material	thickness	filler	frequency range (GHz)	EMI shielding effectiveness (dB)	ref
porous FGS-polystyrene composites	2.5 mm	30 wt %	8.2–12.4	−29	Yan et al.[64]
RGO-poly(ether imide) Films	2.0 μm	0.66 vol %	0.5–8.5	−6.37	Kim et al.[65]
monolayer CVD graphene			2.2–7	−2.27	Hong et al.[66]
GNC-PU composites	1–2 mm	25 wt %	8.2–12.4	−26.45	Kumar et al.[67]
poly(ether imide)/Graphene @ Fe$_3$O$_4$ composite foams	2.5 mm	10 wt %	8–12	−18.2	Shen et al.[68]
graphene−PMMA foam	4.0 mm	1.8 vol %	8–12	−19	Zhang et al.[69]
graphene−wax composites	2.0 mm	20 wt %	2–18	−29.68	Wen et al.[70]
graphene−SiO$_2$ composites	1.5 mm	20 wt %	8.2–12.4	−38	Wen et al.[71]
graphene−epoxy composites		15 wt %	8.2–12.4	−21	Liang et al.[72]
B−N-MRG	1.2 mm		12.4–18	−42	present work
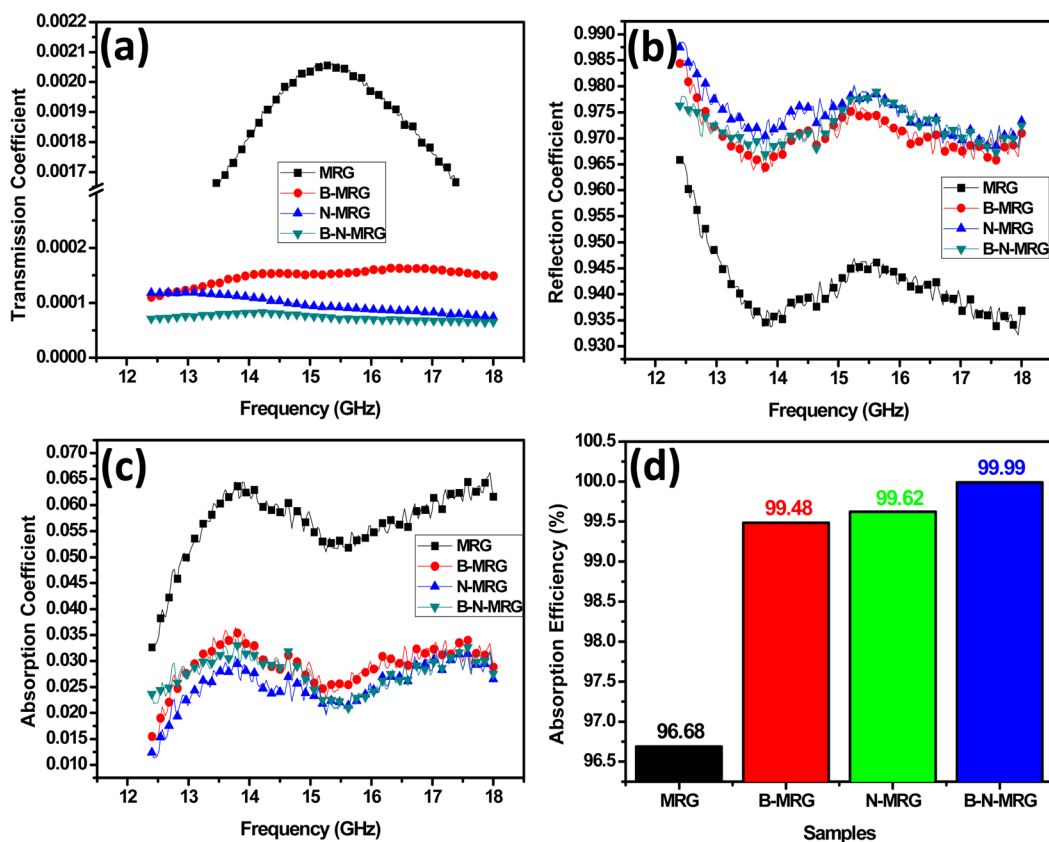
Figure 10. (a) Transmission coefficient, (b) reflection coefficient, (c) absorption coefficient, and (d) absorption efficiency of MRG, B-MRG, N-MRG, and B−N-MRG.

polarization, space charge polarization and natural resonance leading to a high total EMI shielding of −42 dB (∼99.99% attenuation) at mid frequency of 14.8 GHz with a thickness of 1.2 mm and a contribution of −26 dB by SE$_A$ and −16 dB by SE$_R$. Therefore, in the case of B−N-co-doped MRG, the total SE is dominated by the absorption (−26 dB) part, whereas the SE due to reflection (−16 dB) contributes partially.

Further, enhanced microwave shielding due to absorption can be explained in terms of reduction of the skin depth with the doping of B, N, and B−N in MRG. The above results show that shallow skin depths make it possible to attain the same level of attenuation with a thinner shield of the material with different type of doping.[9] The variation of skin depth is shown in Figure 9d with respect to the doping of B, N, and B−N in MRG. The results demonstrate that skin depth is lowest for B−N-MRG, which is responsible for the enhancement of

absorption loss. Thus, for a given thickness, the absorption loss increases with decrease in skin depth.

Table 2 compares the electromagnetic shielding properties of different graphene based materials and composites reported in the literature.

To investigate the microwave attenuation performance of B, N and B−N co-doped MRG, the scattering parameters (S$_{11}$, S$_{21}$) were measured by vector network analyzer to calculate the absorption coefficient (A), reflection coefficient (R), transmittance coefficient (T), and absorption efficiency of the materials. The reflection and transmission coefficient were calculated using scattering parameters as, $R = |E_R/E_I|^2 = |S_{11}|^2 = |S_{22}|^2$ and $T = |E_T/E_I|^2 = |S_{21}|^2 = |S_{12}|^2$. The absorption coefficient and effective absorbance (A_{eff}) was calculated as $A = (1 − R − T)$; $A_{eff} = (1 − R − T)/(1 − R)$, respectively.[73] Figure 10a−c shows the calculated values of transmission,

Scheme 2. Schematic representation of Possible Microwave Absorption Mechanism in B−N−MRG Sample
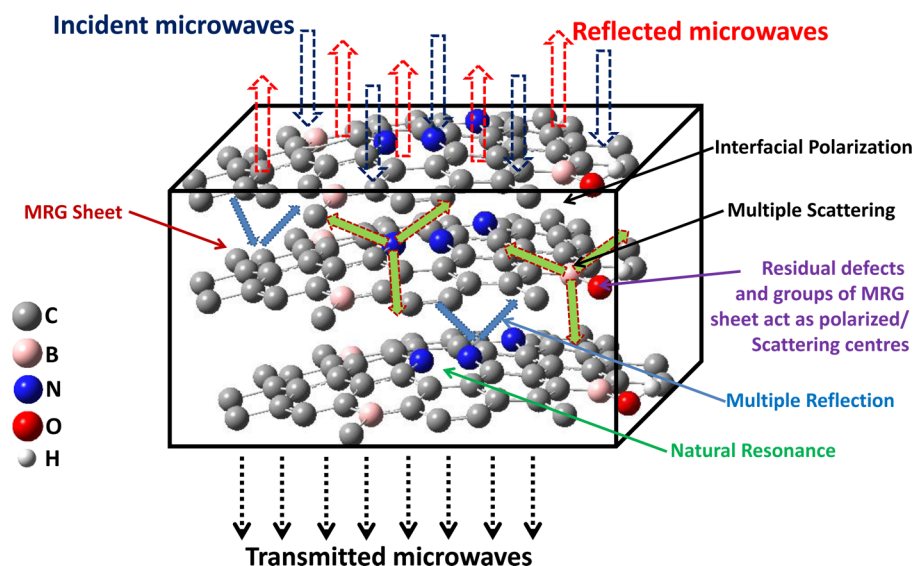
reflection and absorption coefficients for MRG, B-MRG, N-MRG and B−N-MRG, respectively. Figure 10d shows the absorption efficiency values of these materials at thickness of 1.2 mm in the frequency range of 12.4−18 GHz. The transmission coefficient (T) decreases from B, N to B−N doping in MRG and found to be minimum (0.0001) for B−N-MRG.

For all doped samples, the value of T is less than 0.002, as shown in Figure 10a, which is due to the higher value of reflection and absorption coefficients (Figure 10b,c); this proposed that more wave energy is attenuated by B−N-MRG leading to decrease in the T value.

Also, the absorption efficiency of undoped MRG was 96.68% and it reaches up to 99.99% for B−N-MRG at a thickness of 1.2 mm (Figure 10d), that is, 99.99% of EM radiations can be attenuated from the shield.

To further give a visual demonstration of the microwave absorption mechanism as discussed above, a schematic of B−N-MRG sample is given in Scheme 2. From all the above, the results of doping of B, N and both in MRG illustrate that these materials could be used as a microwave absorbing material.

4. CONCLUSION

B, N doped and B−N co-doped MRG have been successfully prepared using microwave assisted method. The detailed microstructural characterizations as well as the characteristics of these doped and undoped materials were examined using SEM, TEM, Raman, XRD, FTIR, and XPS. The highest electrical conductivity of B−N-MRG contributes to shield the EM radiation. Doping of B, N, and B−N in MRG enhanced the interfacial polarization, spin polarization, and natural resonance, which led to high total SE for B−N-MRG ($SE_T \sim -42$ dB, i.e. 99.99% attenuation) in comparison to undoped MRG ($SE_T \sim -28$ dB) at mid frequency region (14.2 GHz) with 1.2 mm thickness. Additionally, the temperature dependent electrical conductivity of MRG, B-MRG, N-MRG and B−N-MRG shows that the thermally activated Arrhenius conduction mechanism is valid only in the high temperature region ($T > 50$ K), whereas Mott's 2D-VRH and ES-VRH mechanisms are valid in the low-temperature region ($T < 50$ K). Thus, the obtained results suggest that this new type of microwave absorption material

can be used in aircraft, defense industries, communication systems, and stealth technology.

■ ASSOCIATED CONTENT

ⓢ Supporting Information

The Supporting Information is available free of charge on the ACS Publications website at DOI: 10.1021/acsami.5b05890.

XPS survey of MRG and B-N-MRG, Table S1 and Table S2 including values of various parameters of 2D-variable range hopping mechanism of all MRG samples, and various parameters of ES-VRH model of all MRG samples (PDF)

■ AUTHOR INFORMATION

Corresponding Author
* Phone: (+091) 542 2307 308. E-mail: anchalbhu@gmail.com.
Author Contributions
§These authors contributed equally.
Notes
The authors declare no competing financial interest.

■ ACKNOWLEDGMENTS

■ REFERENCES

(1) Chen, Z.; Xu, C.; Ma, C.; Ren, W.; Cheng, H. M. Lightweight and Flexible Graphene Foam Composites for High-Performance Electromagnetic Interference Shielding. *Adv. Mater.* **2013**, *25*, 1296−1300.

(2) Gupta, T. K.; Singh, B. P.; Singh, V. N.; Teotia, S.; Singh, A. P.; Elizabeth, I.; Dhakate, S. R.; Dhawan, S.; Mathur, R. MnO₂ decorated graphene nanoribbons with superior permittivity and excellent microwave shielding properties. *J. Mater. Chem. A* **2014**, *2*, 4256−4263.

(3) Chung, D. Carbon materials for structural self-sensing, electromagnetic shielding and thermal interfacing. *Carbon* **2012**, *50*, 3342−3353.

(4) Singh, A. P.; Gupta, B. K.; Mishra, M.; Chandra, A.; Mathur, R.; Dhawan, S. Multiwalled carbon nanotube/cement composites with exceptional electromagnetic interference shielding properties. *Carbon* **2013**, *56*, 86−96.

(5) Singh, A. P.; Mishra, M.; Sambyal, P.; Gupta, B. K.; Singh, B. P.; Chandra, A.; Dhawan, S. K. Encapsulation of γ-Fe₂O₃ decorated reduced graphene oxide in polyaniline core−shell tubes as an exceptional tracker for electromagnetic environmental pollution. *J. Mater. Chem. A* **2014**, *2*, 3581−3593.

(6) Saini, P.; Choudhary, V.; Singh, B. P.; Mathur, R.; Dhawan, S. Polyaniline−MWCNT nanocomposites for microwave absorption and EMI shielding. *Mater. Chem. Phys.* **2009**, *113*, 919−926.

(7) Saini, P.; Choudhary, V.; Dhawan, S. Electrical properties and EMI shielding behavior of highly thermally stable polyaniline/colloidal graphite composites. *Polym. Adv. Technol.* **2009**, *20*, 355−361.

(8) Ling, J.; Zhai, W.; Feng, W.; Shen, B.; Zhang, J.; Zheng, W. G. Facile Preparation of Lightweight Microcellular Polyetherimide/ Graphene Composite Foams for Electromagnetic Interference Shielding. *ACS Appl. Mater. Interfaces* **2013**, *5*, 2677−2684.

(9) Gupta, T. K.; Singh, B. P.; Mathur, R. B.; Dhakate, S. R. Multiwalled carbon nanotube−graphene−polyaniline multiphase nanocomposite with superior electromagnetic shielding effectiveness. *Nanoscale* **2014**, *6*, 842−851.

(10) Gupta, T. K.; Singh, B. P.; Dhakate, S. R.; Singh, V. N.; Mathur, R. B. Improved nanoindentation and microwave shielding properties of modified MWCNT reinforced polyurethane composites. *J. Mater. Chem. A* **2013**, *1*, 9138−9149.

(11) Kumar, R.; Dhakate, S. R.; Gupta, T.; Saini, P.; Singh, B. P.; Mathur, R. B. Effective improvement of the properties of light weight carbon foam by decoration with multi-wall carbon nanotubes. *J. Mater. Chem. A* **2013**, *1*, 5727−5735.

(12) Zhang, H.-B.; Yan, Q.; Zheng, W.-G.; He, Z.; Yu, Z.-Z. Tough Graphene−Polymer Microcellular Foams for Electromagnetic Interference Shielding. *ACS Appl. Mater. Interfaces* **2011**, *3*, 918−924.

(13) Hsiao, S.-T.; Ma, C.-C. M.; Liao, W.-H.; Wang, Y.-S.; Li, S.-M.; Huang, Y.-C.; Yang, R.-B.; Liang, W.-F. Lightweight and Flexible Reduced Graphene Oxide/Water-Borne Polyurethane Composites with High Electrical Conductivity and Excellent Electromagnetic Interference Shielding Performance. *ACS Appl. Mater. Interfaces* **2014**, *6*, 10667−10678.

(14) Gupta, T.; Singh, B. P.; Teotia, S.; Katyal, V.; Dhakate, S.; Mathur, R. Designing of multiwalled carbon nanotubes reinforced polyurethane composites as electromagnetic interference shielding materials. *J. Polym. Res.* **2013**, *20*, 1−7.

(15) Geim, A. K. Graphene: status and prospects. *Science* **2009**, *324*, 1530−1534.

(16) Li, Z.; Wang, J.; Liu, X.; Liu, S.; Ou, J.; Yang, S. Electrostatic layer-by-layer self-assembly multilayer films based on graphene and manganese dioxide sheets as novel electrode materials for supercapacitors. *J. Mater. Chem.* **2011**, *21*, 3397−3403.

(17) Gupta, T. K.; Singh, B. P.; Tripathi, R. K.; Dhakate, S. R.; Singh, V. N.; Panwar, O. S.; Mathur, R. B. Superior nano-mechanical properties of reduced graphene oxide reinforced polyurethane composites. *RSC Adv.* **2015**, *5*, 16921−16930.

(18) Yu, H.; Wang, T.; Wen, B.; Lu, M.; Xu, Z.; Zhu, C.; Chen, Y.; Xue, X.; Sun, C.; Cao, M. Graphene/polyaniline nanorod arrays:

synthesis and excellent electromagnetic absorption properties. *J. Mater. Chem.* **2012**, *22*, 21679−21685.

(19) Wang, C.; Han, X.; Xu, P.; Zhang, X.; Du, Y.; Hu, S.; Wang, J.; Wang, X. The electromagnetic property of chemically reduced graphene oxide and its application as microwave absorbing material. *Appl. Phys. Lett.* **2011**, *98*, 072906.

(20) Wang, X.; Li, X.; Zhang, L.; Yoon, Y.; Weber, P. K.; Wang, H.; Guo, J.; Dai, H. N-doping of graphene through electrothermal reactions with ammonia. *Science* **2009**, *324*, 768−771.

(21) Guo, B.; Liu, Q.; Chen, E.; Zhu, H.; Fang, L.; Gong, J. R. Controllable N-doping of graphene. *Nano Lett.* **2010**, *10*, 4975−4980.

(22) Yang, G.-H.; Zhou, Y.-H.; Wu, J.-J.; Cao, J.-T.; Li, L.-L.; Liu, H.-Y.; Zhu, J.-J. Microwave-assisted synthesis of nitrogen and boron co-doped graphene and its application for enhanced electrochemical detection of hydrogen peroxide. *RSC Adv.* **2013**, *3*, 22597−22604.

(23) Yu, S.; Zheng, W.; Wang, C.; Jiang, Q. Nitrogen/boron doping position dependence of the electronic properties of a triangular graphene. *ACS Nano* **2010**, *4*, 7619−7629.

(24) Charlier, J.-C.; Terrones, M.; Baxendale, M.; Meunier, V.; Zacharia, T.; Rupesinghe, N.; Hsu, W.; Grobert, N.; Terrones, H.; Amaratunga, G. Enhanced electron field emission in B-doped carbon nanotubes. *Nano Lett.* **2002**, *2*, 1191−1195.

(25) Cruz-Silva, E.; Barnett, Z.; Sumpter, B. G.; Meunier, V. Structural, magnetic, and transport properties of substitutionally doped graphene nanoribbons from first principles. *Phys. Rev. B: Condens. Matter Mater. Phys.* **2011**, *83*, 155445.

(26) Panchakarla, L.; Subrahmanyam, K.; Saha, S.; Govindaraj, A.; Krishnamurthy, H.; Waghmare, U.; Rao, C. Synthesis, structure, and properties of boron-and nitrogen-doped graphene. *Adv. Mater.* **2009**, *21*, 4726−4730.

(27) Dai, J.; Yuan, J.; Giannozzi, P. Gas adsorption on graphene doped with B, N, Al, and S: A theoretical study. *Appl. Phys. Lett.* **2009**, *95*, 232105.

(28) Meyer, J. C.; Kurasch, S.; Park, H. J.; Skakalova, V.; Künzel, D.; Groß, A.; Chuvilin, A.; Algara-Siller, G.; Roth, S.; Iwasaki, T. Experimental analysis of charge redistribution due to chemical bonding by high-resolution transmission electron microscopy. *Nat. Mater.* **2011**, *10*, 209−215.

(29) Wang, L.; Yu, P.; Zhao, L.; Tian, C.; Zhao, D.; Zhou, W.; Yin, J.; Wang, R.; Fu, H. B and N isolate-doped graphitic carbon nanosheets from nitrogen-containing ion-exchanged resins for enhanced oxygen reduction. *Sci. Rep.* **2014**, *4*, 5184.

(30) Wang, X.; Sun, G.; Routh, P.; Kim, D.-H.; Huang, W.; Chen, P. Heteroatom-doped graphene materials: syntheses, properties and applications. *Chem. Soc. Rev.* **2014**, *43*, 7067−7098.

(31) Lv, R.; Li, Q.; Botello-Méndez, A. R.; Hayashi, T.; Wang, B.; Berkdemir, A.; Hao, Q.; Elías, A. L.; Cruz-Silva, R.; Gutiérrez, H. R. Nitrogen-doped graphene: beyond single substitution and enhanced molecular sensing. *Sci. Rep.* **2012**, *2*, 586.

(32) Xue, Y.; Yu, D.; Dai, L.; Wang, R.; Li, D.; Roy, A.; Lu, F.; Chen, H.; Liu, Y.; Qu, J. Three-dimensional B, N-doped graphene foam as a metal-free catalyst for oxygen reduction reaction. *Phys. Chem. Chem. Phys.* **2013**, *15*, 12220−12226.

(33) Xing, M.; Shen, F.; Qiu, B.; Zhang, J. Highly-dispersed Boron-doped Graphene Nanosheets Loaded with TiO₂ Nanoparticles for Enhancing CO₂ Photoreduction. *Sci. Rep.* **2014**, *4*, 6341.

(34) Zhu, J.; He, C.; Li, Y.; Kang, S.; Shen, P. K. One-step synthesis of boron and nitrogen-dual-self-doped graphene sheets as non-metal catalysts for oxygen reduction reaction. *J. Mater. Chem. A* **2013**, *1*, 14700−14705.

(35) Marcano, D. C.; Kosynkin, D. V.; Berlin, J. M.; Sinitskii, A.; Sun, Z.; Slesarev, A.; Alemany, L. B.; Lu, W.; Tour, J. M. Improved synthesis of graphene oxide. *ACS Nano* **2010**, *4*, 4806−4814.

(36) Zheng, Y.; Jiao, Y.; Ge, L.; Jaroniec, M.; Qiao, S. Z. Two-Step Boron and Nitrogen Doping in Graphene for Enhanced Synergistic Catalysis. *Angew. Chem., Int. Ed.* **2013**, *52*, 3110−3116.

(37) Li, Z.; Lu, C.; Xia, Z.; Zhou, Y.; Luo, Z. X-ray diffraction patterns of graphite and turbostratic carbon. *Carbon* **2007**, *45*, 1686−1695.

(38) Cullity, B. *Elements of X-ray Diffraction*. 2nd ed. ed.; Addison-Wesley Publishing Company, Reading, MA, 1978.

(39) Umrao, S.; Abraham, S.; Theil, F.; Pandey, S.; Ciobota, V.; Shukla, P. K.; Rupp, C. J.; Chakraborty, S.; Ahuja, R.; Popp, J. A possible mechanism for the emergence of an additional band gap due to a Ti−O−C bond in the TiO$_2$−graphene hybrid system for enhanced photodegradation of methylene blue under visible light. *RSC Adv.* **2014**, *4*, 59890−59901.

(40) Reddy, A. L. M.; Srivastava, A.; Gowda, S. R.; Gullapalli, H.; Dubey, M.; Ajayan, P. M. Synthesis of nitrogen-doped graphene films for lithium battery application. *ACS Nano* **2010**, *4*, 6337−6342.

(41) Ferrari, A.; Robertson, J. Interpretation of Raman spectra of disordered and amorphous carbon. *Phys. Rev. B: Condens. Matter Mater. Phys.* **2000**, *61*, 14095.

(42) Barros, E.; Demir, N.; Souza Filho, A.; Mendes Filho, J.; Jorio, A.; Dresselhaus, G.; Dresselhaus, M. Raman spectroscopy of graphitic foams. *Phys. Rev. B: Condens. Matter Mater. Phys.* **2005**, *71*, 165422.

(43) Cançado, L. G.; Jorio, A.; Ferreira, E. M.; Stavale, F.; Achete, C.; Capaz, R.; Moutinho, M.; Lombardo, A.; Kulmala, T.; Ferrari, A. Quantifying defects in graphene via Raman spectroscopy at different excitation energies. *Nano Lett.* **2011**, *11*, 3190−3196.

(44) Dresselhaus, M. S.; Dresselhaus, G. Intercalation compounds of graphite. *Adv. Phys.* **2002**, *51*, 1−186.

(45) Enoki, T.; Endo, M.; Suzuki, M. *Graphite Intercalation Compounds and Applications*. Oxford University Press: Oxford, 2003.

(46) Das, A.; Chakraborty, B.; Piscanec, S.; Pisana, S.; Sood, A.; Ferrari, A. Phonon renormalization in doped bilayer graphene. *Phys. Rev. B: Condens. Matter Mater. Phys.* **2009**, *79*, 155417.

(47) Das, A.; Pisana, S.; Chakraborty, B.; Piscanec, S.; Saha, S.; Waghmare, U.; Novoselov, K.; Krishnamurthy, H.; Geim, A.; Ferrari, A. Monitoring dopants by Raman scattering in an electrochemically top-gated graphene transistor. *Nat. Nanotechnol.* **2008**, *3*, 210−215.

(48) Pietronero, L.; Strässler, S. Bond-length change as a tool to determine charge transfer and electron-phonon coupling in graphite intercalation compounds. *Phys. Rev. Lett.* **1981**, *47*, 593.

(49) Piscanec, S.; Lazzeri, M.; Mauri, F.; Ferrari, A.; Robertson, J. Kohn anomalies and electron-phonon interactions in graphite. *Phys. Rev. Lett.* **2004**, *93*, 185503.

(50) Pisana, S.; Lazzeri, M.; Casiraghi, C.; Novoselov, K. S.; Geim, A. K.; Ferrari, A. C.; Mauri, F. Breakdown of the adiabatic Born−Oppenheimer approximation in graphene. *Nat. Mater.* **2007**, *6*, 198−201.

(51) Basko, D.; Piscanec, S.; Ferrari, A. Electron-electron interactions and doping dependence of the two-phonon Raman intensity in graphene. *Phys. Rev. B: Condens. Matter Mater. Phys.* **2009**, *80*, 165413.

(52) Basko, D. M. Theory of resonant multiphonon Raman scattering in graphene. *Phys. Rev. B: Condens. Matter Mater. Phys.* **2008**, *78*, 125418.

(53) Lazzeri, M.; Mauri, F. Nonadiabatic Kohn anomaly in a doped graphene monolayer. *Phys. Rev. Lett.* **2006**, *97*, 266407.

(54) Cancado, L.; Takai, K.; Enoki, T.; Endo, M.; Kim, Y.; Mizusaki, H.; Jorio, A.; Coelho, L.; Magalhaes-Paniago, R.; Pimenta, M. General equation for the determination of the crystallite size L a of nanographite by Raman spectroscopy. *Appl. Phys. Lett.* **2006**, *88*, 163106.

(55) Yang, Q.-H.; Hou, P.-X.; Unno, M.; Yamauchi, S.; Saito, R.; Kyotani, T. Dual Raman features of double coaxial carbon nanotubes with N-doped and B-doped multiwalls. *Nano Lett.* **2005**, *5*, 2465−2469.

(56) Sun, C.-L.; Wang, H.-W.; Hayashi, M.; Chen, L.-C.; Chen, K.-H. Atomic-scale deformation in N-doped carbon nanotubes. *J. Am. Chem. Soc.* **2006**, *128*, 8368−8369.

(57) Mott, N. F.; Davis, E. A. *Electronic Processes in Non-Crystalline Materials*. Oxford University Press: Oxford, 2012.

(58) Khan, Z. H.; Husain, M.; Perng, T.; Salah, N.; Habib, S. Electrical transport via variable range hopping in an individual multi-wall carbon nanotube. *J. Phys.: Condens. Matter* **2008**, *20*, 475207.

(59) Lee, S.; Ketterson, J.; Trivedi, N. Metal-insulator transition in quasi-two-dimensional Mo-C films. *Phys. Rev. B: Condens. Matter Mater. Phys.* **1992**, *46*, 12695.

(60) Muchharla, B.; Narayanan, T.; Balakrishnan, K.; Ajayan, P. M.; Talapatra, S. Temperature dependent electrical transport of disordered reduced graphene oxide. *2D Mater.* **2014**, *1*, 011008.

(61) Peters, E.; Giesbers, A.; Burghard, M. Variable range hopping in graphene antidot lattices. *Phys. Status Solidi B* **2012**, *249*, 2522−2525.

(62) Joung, D.; Chunder, A.; Zhai, L.; Khondaker, S. I. Space charge limited conduction with exponential trap distribution in reduced graphene oxide sheets. *Appl. Phys. Lett.* **2010**, *97*, 093105.

(63) Singh, K.; Ohlan, A.; Pham, V. H.; Balasubramaniyan, R.; Varshney, S.; Jang, J.; Hur, S. H.; Choi, W. M.; Kumar, M.; Dhawan, S. Nanostructured graphene/Fe$_3$O$_4$ incorporated polyaniline as a high performance shield against electromagnetic pollution. *Nanoscale* **2013**, *5*, 2411−2420.

(64) Yan, D.-X.; Ren, P.-G.; Pang, H.; Fu, Q.; Yang, M.-B.; Li, Z.-M. Efficient electromagnetic interference shielding of lightweight graphene/polystyrene composite. *J. Mater. Chem.* **2012**, *22*, 18772−18774.

(65) Kim, S.; Oh, J.-S.; Kim, M.-G.; Jang, W.; Wang, M.; Kim, Y.; Seo, H. W.; Kim, Y. C.; Lee, J.-H.; Lee, Y. Electromagnetic Interference (EMI) Transparent Shielding of Reduced Graphene Oxide (RGO) Interleaved Structure Fabricated by Electrophoretic Deposition. *ACS Appl. Mater. Interfaces* **2014**, *6*, 17647−17653.

(66) Hong, S. K.; Kim, K. Y.; Kim, T. Y.; Kim, J. H.; Park, S. W.; Kim, J. H.; Cho, B. J. Electromagnetic interference shielding effectiveness of monolayer graphene. *Nanotechnology* **2012**, *23*, 455704.

(67) Kumar, A.; Alegaonkar, P. S. Impressive Transmission Mode Electromagnetic Interference Shielding Parameters of Graphene-like Nanocarbon/Polyurethane Nanocomposites for Short Range Tracking Countermeasures. *ACS Appl. Mater. Interfaces* **2015**, *7*, 14833−14842.

(68) Shen, B.; Zhai, W.; Tao, M.; Ling, J.; Zheng, W. Lightweight, multifunctional polyetherimide/graphene@ Fe3O4 composite foams for shielding of electromagnetic pollution. *ACS Appl. Mater. Interfaces* **2013**, *5*, 11383−11391.

(69) Zhang, H.-B.; Yan, Q.; Zheng, W.-G.; He, Z.; Yu, Z.-Z. Tough graphene− polymer microcellular foams for electromagnetic interference shielding. *ACS Appl. Mater. Interfaces* **2011**, *3*, 918−924.

(70) Wen, B.; Wang, X.; Cao, W.; Shi, H.; Lu, M.; Wang, G.; Jin, H.; Wang, W.; Yuan, J.; Cao, M. Reduced graphene oxides: the thinnest and most lightweight materials with highly efficient microwave attenuation performances of the carbon world. *Nanoscale* **2014**, *6*, 5754−5761.

(71) Wen, B.; Cao, M.; Lu, M.; Cao, W.; Shi, H.; Liu, J.; Wang, X.; Jin, H.; Fang, X.; Wang, W. Reduced Graphene Oxides: Light-Weight and High-Efficiency Electromagnetic Interference Shielding at Elevated Temperatures. *Adv. Mater.* **2014**, *26*, 3484−3489.

(72) Liang, J.; Wang, Y.; Huang, Y.; Ma, Y.; Liu, Z.; Cai, J.; Zhang, C.; Gao, H.; Chen, Y. Electromagnetic interference shielding of graphene/epoxy composites. *Carbon* **2009**, *47*, 922−925.

(73) Mishra, M.; Singh, A. P.; Singh, B.; Singh, V.; Dhawan, S. Conducting ferrofluid: a high-performance microwave shielding material. *J. Mater. Chem. A* **2014**, *2*, 13159−13168.